Enhanced daytime secondary aerosol formation driven by gas-particle partitioning in downwind urban plumes

Mingfu Cai[1,2,3], Ye Chenshuo[4], Bin Yuan[2,3*], Shan Huang[2,3], E Zheng[2,3], Suxia Yang[5], Zelong Wang[2,3], Yi Lin[2,3], Tiange Li [2,3], Weiwei Hu[6], Wei Chen[6], Qicong Song[2,3], Wei Li[2,3], Yuwen Peng[2,3], Baoling Liang[7], Qibin Sun[7], Jun Zhao[7], Duohong Chen[8], Jiaren Sun[1], Zhiyong Yang[9], Min Shao[2,3]

[1]Guangdong Province Engineering Laboratory for Air Pollution Control, Guangdong Provincial Key Laboratory of Water and Air Pollution Control, South China Institute of Environmental Sciences, MEE, Guangzhou 510655, China

[2]Institute for Environmental and Climate Research, Jinan University, Guangzhou 51143, China

[3]Guangdong-Hongkong-Macau Joint Laboratory of Collaborative Innovation for Environmental Quality, Jinan University, Guangzhou 510632, China

[4] Guangdong Provincial Academy of Environmental Science, Guangzhou, 510045, China

[5] Guangzhou Research Institute of Environment Protection Co.,Ltd, Guangzhou 510620, China

[6]State Key Laboratory of Organic Geochemistry and Guangdong Key Laboratory of Environmental Protection and Resources Utilization, Guangzhou Institute of Geochemistry, Chinese Academy of Sciences, Guangzhou 510640, China

[7]School of Atmospheric Sciences, Guangdong Province Key Laboratory for Climate Change and Natural Disaster Studies, and Institute of Earth Climate and Environment System, Sun Yat-sen University, Zhuhai 519082, China

[8]Guangdong Environmental Monitoring Center, Guangzhou 510308, China

[9]Guangzhou Huangpu District Meteorological Bureau, Guangzhou 510530, China

Corresponding authors: Bin Yuan (byuan@jnu.edu.cn)

Abstract.

Anthropogenic emissions from city clusters can significantly enhance secondary organic aerosol (SOA) formation in the downwind regions, while the mechanism is poorly understood. To investigate the effect of pollutants within urban plumes on organic aerosol (OA) evolution, a field campaign was conducted at a downwind site of the Pearl River Delta region of China in the fall of 2019. A time-of-flight chemical ionization mass spectrometer coupled with a Filter Inlet for Gases and Aerosol (FIGAERO-CIMS) was used to probe the gas- and particle-phase molecular composition and thermograms of organic compounds. For air masses influenced by urban pollution, strong daytime SOA formation through gas-particle partitioning was observed, resulting in higher OA volatility. The obvious SOA enhancement was mainly attributed to the gas-particle partitioning of high volatility (SVOC+IVOC+VOC, $C^* > 0.3$ μg m^{-3}) organic vapors. Using the equilibrium equation could underestimate the contribution of high volatility organic vapors, since the volatility of these species in the particle-phase was lower than that in the gas-phase. We speculated that the elevated NO$_x$ concentration could suppress the formation of highly oxidized products, resulting in a smooth increase of low volatility (ELVOC+LVOC, $C^* \leq 0.3$ μg m^{-3}) organic vapors. Evidences showed that urban pollutants (NO$_x$ and VOCs) could enhance the oxidizing capacity, while the elevated VOCs were mainly responsible for promoting daytime SOA formation by increasing the RO$_2$ production rate. Our results highlight the important role of urban anthropogenic pollutants in SOA control in the suburban region.

1. Introduction

As a major concern of air pollution, aerosol particles are known to have significant impacts on public health and climate (Apte et al., 2018; Arias et al., In Press). Primary particulate matter (PM) in China has shown a remarkable reduction since 2013, owing to strictly clean air policies implemented by the Chinese government (Zhang et al., 2019). Despite the effective reduction of primary emissions in the past ten years, secondary organic aerosol (SOA) remains at high levels and is mainly responsible for the haze development in China(Huang et al., 2014). SOA is thought to be formed through the oxidation of volatile organic compounds (VOCs) and atmospheric aging processes of primary organic aerosol (POA). However, models are especially challenged in reproducing SOA concentration and properties, since the formation mechanisms and gas precursors of SOA remain poorly characterized(Hodzic et al., 2010).

Gas-particle partitioning of organic vapors is found to be the important formation pathway of SOA the worldwide(Nie et al., 2022; Hallquist et al., 2009; Lanzafame et al., 2021). Nie et al. (2022) suggested that the contribution of the condensation of organic vapors to the SOA mass growth ranged from about 38%-71% in China megacities. Photochemical produced SOA via gas phase chemistry is usually related to a higher volatility and a lower oxidation degree than that formed in the aqueous phase (Ervens et al., 2011; Saha et al., 2017). The condensation processes of organic vapors are determined by their volatility, which is closely related to oxidation state, functional groups, and the number of atomic carbons. Laboratory studies revealed that high nitrogen oxides (NO_x) concentration can suppress the production of molecules with high oxidation degree by inhibiting autoxidation(Rissanen, 2018; Peng et al., 2019), which is considered to be an important pathway of low volatility vapor formation(Praske et al., 2018). Such compounds have been shown to play a vital role in the SOA formation and growth of newly formed particles(Mutzel et al., 2015; Bianchi et al., 2019; Mohr et al., 2019). On the other hand, it is shown that the increase of oxidant owing to elevated NO_x concentration can offset the decrease of autoxidation efficiency, leading to a higher production of oxygenated organic vapors(Pye et al., 2019), highlighting the complexity of SOA formation. However, the lack of a molecular dataset of SOA and gas precursors hinders the understanding of the SOA formation mechanism.

Recently, a chemical ionization time-of-flight mass spectrometer coupled with a Filter Inter for

74 Gases and AEROsols (FIGAERO-CIMS) has been employed to measure gas- and particle-phase

75 oxygenated organic compounds the worldwide (Chen et al., 2020; Buchholz et al., 2020; Masoud et

76 al., 2022). Using a FIGAERO-CIMS, Cai et al. (2023) showed that heterogeneous reaction might

77 have an important role in the secondary formation of particle-phase oxidized organic nitrogen. The

78 volatility of OA can provide information about the formation and aging processes of OA, given that

79 it is strongly affected by chemical composition. In past decades, a thermodenuder (TD) coupled

80 with aerosol detection instruments (e.g. aerosol mass spectrometer and condensation particle

81 counter) was widely used in the estimation of OA volatility (Philippin et al., 2004; Lee et al., 2010).

82 Cai et al. (2022) found that the OA volatility was higher at a particle size range of 30 to 200 nm

83 during daytime, suggesting that the SOA formation through gas-particle partitioning could generally

84 occur at all particle sizes. However, this method failed to provide the volatility information of

85 different molecules of OA. In recent years, the FIGAERO-CIMS was developed to characterize the

86 volatility of oxygenated organic molecules in the particle phase. (Ren et al., 2022; Ylisirniö et al.,

87 2020). Wang and Hildebrandt Ruiz (2018) showed that the thermal desorption products of SOA can

88 be separated into different groups on a two-dimensional thermogram measured by the FIGAERO-

89 CIMS. Ren et al. (2022) investigated the relationship between the molecular formulae of OA

90 components and their volatilities and suggested that the volatility of OA compounds was strongly

91 affected by O to C ratio. These results provide valuable insights into the SOA formation mechanisms.

92 However, as yet few FIAGERO-CIMS field studies are available in the literature in China(Ye et al.,

93 2021; Salvador et al., 2021), especially in urban downwind areas.

94   Observational studies have demonstrated that anthropogenic emissions can significantly affect

95 SOA formation in the downwind region. Fry et al. (2018) observed an enhancement of organic

96 nitrate aerosol formed through NO_3+isoprene in power plant plume during nighttime, which was

97 mainly attributed to NO_x emissions from the power plant. The results from Liu et al. (2018)

98 suggested that the OH concentrations increased by at least 250% under polluted conditions, which

99 might promote the daytime SOA formation. A field measurement in the Amazon forest by De Sá et

100 al. (2018) showed that the enhancement of OA (about 30-171%) in urban plumes was mainly

101 contributed by SOA. A recent study founded that anthropogenic emission of NO_x from urban could

102 enhance oxidant concentration, thereby promoting daytime SOA formation(Shrivastava et al., 2019).

103   In this study, we investigate the SOA formation through photochemical reactions at a typical

104 downwind site in the Pearl River Delta region (PRD) using a FIGAERO-CIMS along with a suite

105 of other online instruments. The volatility of OA and its relationship with identified OA sources

106 during long-range transport, urban air masses, and coastal air masses periods are discussed. The

107 formation mechanisms of daytime SOA formation within the urban plume are investigated based on

108 online measurements of gas- and particle-phase organic compounds, gaseous pollutants, and aerosol

109 physicochemical properties. The impact of urban pollutants on SOA formation will be discussed.

110 2. Measurement and Method

111 2.1 Field measurement

112 The campaign was conducted at the Heshan supersite in the PRD region during the fall of 2019

113 (29th September to 17th November 2019). The Heshan Supersite, surrounded by farms and villages,

114 is located (at 22°42′39. 1″N, 112°55′35.9″E, with an altitude of about 40 m) at southwest of the

115 PRD region and about 70 km southwest of Guangzhou city (Fig. S1). During the measurement, the

116 sampling site is mainly influenced by the air masses from the center of the PRD region (Fig. S2a).

117 All instruments were placed in an air-conditioned room on the top floor of the supersite. A detailed

118 description of the site and experimental setup can be found in Cai et al. (2021).

119 2.2 Instrumentation

120 2.2.1 FIGAERO-CIMS

121 A FIGAERO-CIMS coupled with an X-ray source was employed to measure organic

122 compounds in the gas- and particle-phase using I^- as the chemical ionization reagent. The particle

123 sampling inlet of the FIGAERO-CIMS was equipped with a $PM_{2.5}$ cyclone and a Nafion dryer

124 (model PD-07018T-12MSS, Perma Pure, Inc., USA). The principle of the instrument can be found

125 in Lopez-Hilfiker et al. (2014) and Le Breton et al. (2018). In general, the operation settings and

126 data processing were the same as Cai et al. (2023) and Ye et al. (2021). Here, only a brief description

127 relevant to the measurement is given. The instrument was worked in a cycle pattern of 1 hour, with

128 24 minutes of gas-phase measurements and particle collection (sampling mode), followed by a 36-

129 minutes particle-phase analysis (desorption mode). In the sampling mode, ambient gas was

130 measured in the first 21 minutes, followed by a 3-min zero air background. At the same time,

131 ambient particles were collected on a PTFE membrane filter. In the desorption mode, the collected

132 particles were desorbed by heated N_2. The temperature of the N_2 was linearly ramped from indoor

133 temperature (~25°C) to ~175 °C in 12 minutes and held for 24 minutes. The data processing steps

134 in this campaign were the same as Ye et al. (2021). A few chemicals were calibrated before and after

135 the measurement. For uncalibrated species, a voltage scanning method was employed to obtain their

136 sensitivities (referred to as semi-quantified species) (Ye et al., 2021; Iyer et al., 2016; Lopez-Hilfiker

137 et al., 2016).

138 **2.2.2 SP-AMS**

139   The PM_1 chemical composition was measured by a soot particle aerosol mass spectrometer

140 (SP-AMS, Aerodyne Research, Inc., USA). The details of the operation and data analysis can be

141 found in Kuang et al. (2021). Source apportionment was performed for organic aerosols in the bulk

142 PM_1 using positive matrix factorization (PMF). The organic aerosol could be divided into six

143 components, including two primary OA factors and four secondary OA factors. The mass spectral

144 profiles of six OA factors are shown in Figure S3. The timeseries and diurnal variation of these

145 factors are presented in Figure S4.

146   The primary OA factors include hydrocarbon-like OA (HOA), mainly contributed by traffic

147 and cooking emissions and biomass burning OA (BBOA) originating from biomass burning

148 combustion. The HOA was identified by hydrocarbon ions $C_xH_y^+$. Owing to the prominent

149 hydrocarbon ions and low O:C value (0.10), HOA could be attributed to primary emission from

150 cooking and traffic. The BBOA was recognized by the markers $C_2H_4O_2^+$ (m/z 60.022, 0.5%) and

151 $C_3H_5O_2^+$ (m/z 73.029, 0.4%), which are considered tracers for biomass burning OA (Ng et al., 2011).

152   The SOA factors include biomass burning SOA (BBSOA) likely formed from oxidation of

153 biomass burning emission, less oxygenated OA (LOOA) provided by strong daytime photochemical

154 formation, more oxygenated OA (MOOA) related to regional transport, and nighttime-formed OA

155 (Night-OA) contributed by secondary formation during nighttime. The BBSOA was likely formed

156 through oxidation of biomass burning precursors, which was supported by the evening peak at about

157 19:00 LT (Fig. S4). BBSOA showed a similar variation trend with $C_6H_2NO_4^+$, which might be

158   contributed by oxidation of gaseous precursors from biomass burning emissions (Wang et al., 2019;

159   Bertrand et al., 2018). The significant afternoon peak of LOOA indicates its formation through

160   photochemical reactions, which would be detailly discussed in section 3.1. The negligible diurnal

161   variation and the highest O:C value (1.0) of MOOA suggested that it could be aged OA resulting

162   from long-range transport. Night-OA was formed through NO_3 nighttime chemistry, supported by

163   a pronounced evening elevation and positive correlation with nitrate (R=0.67).The detailed

164   determination of PMF factors has been found in Kuang et al. (2021) and Luo et al. (2022).

165   **2.2.3 Particle number size distribution measurements**

166   Particle number size distribution in a size range of 1 nm - 10 μm was measured by a diethylene

167   glycol scanning mobility particle sizer (DEG-SMPS, model 3938E77, TSI Inc., USA), a SMPS

168   (model 3938L75, TSI Inc., USA), and an aerodynamic particle sizer (APS, model 3321, TSI Inc.,

169   USA). All sample particles first passed through a Nafion dryer (Model MD-700, Perma Pure Inc.,

170   USA) to reduce relative humidity (RH) lower than 30%. A detailed description of these instruments

171   can be found in Cai et al. (2021).

172   **2.2.4 Other parameters**

173   The non-methane hydrocarbons（NMHC）were measured by an online GC-MS-FID (Wuhan

174   Tianhong Co., Ltd, China). The concentration of oxygenated VOCs, including formaldehyde

175   (HCHO) and acetaldehyde (CH_3CHO), were measured using high-resolution proton transfer

176   reaction time-of-flight mass spectrometry (PTR-ToF-MS, Ionicon Analytik, Austria). HONO was

177   detected by the gas and aerosol collector (GAC) instrument (Dong et al., 2012). Trace gases,

178   including O_3, NO_x, and CO, were measured by gas analyzers (model 49i, 42i, and 48i, Thermo

179   Scientific, US). Meteorological parameters (i.e., wind speed, wind direction, and temperature) were

180   measured by a weather station (Vantage Pro 2, Davis Instruments Co., US).

181   **2.3 Methodology**

182   **2.3.1 Estimation of the volatility of particle- and gas-phase organic compounds**

183   During the heating processes, the FIGAERO-CIMS simultaneously measured the desorbing

184 compounds of the collected particles. Thus, the volatility information of particles can be obtained

185 by investigating the relationship between the measured signals and desorption temperature. The

186 temperature of the peak desorption signal (T_{max}) has a nearly linear relationship with the natural

187 logarithm of saturation vapor pressure (P_{sat}) of the respective compound (Lopez-Hilfiker et al.,

188 2014):

189 $\qquad ln(P_{sat}) = aT_{max} + b \qquad\qquad\qquad\qquad\qquad\qquad\qquad\qquad (1)$

190 where a and b are fitting coefficients. Thus, saturation vapor concentration (C^*, µg m^{-3}) can be

191 obtained:

192 $\qquad C^* = \frac{P_{sat}M_w}{RT}10^6 \qquad\qquad\qquad\qquad\qquad\qquad\qquad\qquad (2)$

193 where M_w is the molecular weight of the compound (determined by the FIGAERO-CIMS), R is the

194 universal gas constant (8.314 J mol^{-1} K^{-1}), and T is the thermodynamic temperature in kelvin (298.15

195 K).

196 $\qquad$ We used a series of polyethylene glycol (PEG 5-8) compounds to calibrate the T_{max} and

197 obtained the fitting parameters a and b. The PEG standards were prepared in a mixture of

198 acetonitrile and then atomized with a homemade atomizer. The atomized particles are classified by

199 a differential mobility analyzer (DMA, model 3081 L, TSI Inc., USA) at two diameters (100 nm

200 and 200 nm). The selected particles were then split into two paths: one to a condensation particle

201 counter (CPC, model 3775, TSI Inc., USA) for measuring the particle concentration and another

202 one to the particle inlet of the FIGAERO-CIMS. The collected concentration can be calculated based

203 on the selected particle diameter, particle number concentration, flow rate of the particle inlet of

204 FIGAERO-CIMS, and collection time. The calibration results and corresponding fitting parameters

205 can be found in Fig. S5 and Table. S1. Note that the T_{max} can vary with mass loading, and it is

206 necessary to consider for estimation the relationship between T_{max} and C^* (Wang and Hildebrandt

207 Ruiz, 2018). Our calibration results demonstrated that the correlation between T_{max} shift and mass

208 loading was not linear, which may be attributed to matrix or saturation effects (Huang et al., 2018).

209 During the measurement, the collected mass loading centered at about 620 ng and the particle

210 volume size distribution (PVSD) centered at about 400 nm (Fig. S6). Thus, the fitting parameters

211 (a=-0.206 and a=3.732) of the calibration experiment with a diameter of 200 nm and mass loading

212 of 407 ng were adopted in the C^* calculation, since the mass loading and diameter are the closest to

213   the ambient samples.

214   For gas-phase organic compounds (organic vapors), we first divided them into two groups

215   based on their oxidation pathways (multi-generation OH oxidation and autoxidation, solid line in

216   Fig. S7) and then used different parameters in their volatility estimation. The classification of

217   pathways was based on the molecular characteristics of oxidation products of aromatics and

218   monoterpene, respectively (Wang et al., 2020). In general, their saturation vapor concentration (C^*,

219   at 300 K) can be estimated as follows:

220   $$log_{10}(C^*(300K)) = (25 - n_c) \cdot b_C - (n_O - 3n_N) \cdot b_O - \frac{2(n_O - 3n_N)n_C}{(n_C + n_O - 3n_N)} \cdot b_{CO} - n_N \cdot b_N \quad (3)$$

221   where n_c, n_O, and n_N are the numbers of carbon, oxygen, and nitrogen atoms in each compound.

222   For oxidation products formed from multi-generation OH oxidation (aging) pathway, the volatility

223   parameters b_C, b_O, b_{CO}, and b_N were assumed to be 0.475, 2.3, -0.3, and 2.5, respectively (Donahue

224   et al., 2011). For oxidation products formed from autoxidation pathway, the modified

225   parameterization is used, with b_C=0.475, b_O=0.2, b_{CO}=0.9, and b_N =2.5 (Bianchi et al., 2019). It

226   should be noted that this method can only roughly distinguish the formation pathways of ambient

227   organic vapors, since it is based on the oxidation products of specific species in a laboratory study.

2.3.2 Calculation of oxidation state ($\overline{OS_C}$) of $C_xH_yO_z$ and $C_xH_yN_{1,2}O_z$ compounds

229   For $C_xH_yO_z$ compounds, the $\overline{OS_C}$ can be estimated as:

230   $$\overline{OS_C} = 2 \times \frac{O}{C} - \frac{H}{C} \quad (4)$$

231   For $C_xH_yN_{1,2}O_z$ compounds, the $\overline{OS_C}$ can be calculated from following equation:

232   $$\overline{OS_C} = 2 \times \frac{O}{C} - \frac{H}{C} - x \times \frac{N}{C} \quad (5)$$

233   where x is the valence state of N atoms, which is dependent on functional groups. Several

234   assumptions were adopted to classify them. (1)N-containing functional groups were nitro (-NO$_2$,

235   x=+3) or nitrate (-NO$_3$, x=+5) in our measurement; (2)N-containing aromatics contain nitro

236   moieties while N-containing aliphatic hydrocarbons contain nitrate moieties; (3)N-containing

237   aromatics have 6-9 carbon atoms and fewer hydrogen atoms than aliphatic hydrocarbons with the

238   same number of carbon atoms.

239   **2.3.3 Estimation of condensation sink**

240   The condensation sink (CS) represents the condensing vapor captured by pre-existing particles

241   and can be calculated from the following equation:

242    $CS = 2\pi D \sum_{D_p} \beta_{m,D_p} D_p N_{D_p}$ (6)

243   where D is the diffusion coefficient of the H_2SO_4 vapor (0.8×10^{-5} m^2 s^{-1}), β_{m,D_p} is the

244   transitional regime correction factor which can be calculated from the Knudsen number (Fuchs and

245   Sutugin, 1971), and N_{D_p} represents the particle number concentration at D_p.

246   **2.3.4 Estimation of OA contributed by high volatility organic vapors**

247   Organic vapors with higher volatility (SVOC+IVOC+VOC, $C^* >0.3$ µg m^{-3}) can easily reach

248   an equilibrium between the gas and particle phase. Thus, the contribution of high volatility organic

249   vapors to OA concentration (OA_{HVgas}) through gas-particle partitioning can be estimated as

250   following:

251    $OA_{HVgas} = \sum_i C_{i,g} f_i$ (7)

252   where $C_{i,g}$ is the gas-phase concentration of species i. f_i is the fraction of species i in the particle

253   phase and is defined as:

254    $f_i = \frac{C_{OA}}{C_{OA}+C_i^*(T)}$ (8)

255   where C_{OA} is the concentration of OA measured by the SP-AMS, and $C_i^*(T)$ is the saturation

256   concentration of species i at temperature (T). The temperature-dependent $C_i^*(T)$ was obtained by

257   (Nie et al., 2022):

258    $\log_{10} C_i^*(T) = \log_{10} C_i^*(300K) + \frac{\Delta H_{vap,i}}{Rln(10)}(\frac{1}{300} - \frac{1}{T})$ (9)

259    $\Delta H_{vap,i}$=-5.7$\log_{10} C_i^*(300K)$+129   (10)

260   where $\Delta H_{vap,i}$ is the enthalpy of vaporization and can be estimated based on $\log_{10} C_i^*(300K)$.

261   **2.3.4 Estimation of the production rate of RO$_2$ and OH**

262   A zero-dimensional box model (0-D Atmospheric Modeling, F0AM(Wolfe et al., 2016)) based

263   on Master Chemical Mechanism (MCM v3.1.1, https://mcm.york.ac.uk/MCM) was used to simulate

264   the production rate of OH in this study. The F0AM box model has been widely used in investigating

265 chemical reactions of VOCs, NOx, and RO$_x$ radicals (including OH, HO$_2$, and RO$_2$) in field and

266 laboratory researches (Baublitz et al., 2023; Yang et al., 2022; D'ambro et al., 2017). The simulation

267 was constrained with the observation data of non-methane hydrocarbons (NMHC), HCHO,

268 CH$_3$CHO, NO, CO, HONO, and meteorological parameters (RH, temperature, photolysis rates, and

269 pressure). The background concentration of CH$_4$ was set as 1.8 ppm (Wang et al., 2011). The

270 simulation time step was set to be 5 minutes. With respect to the integrity and temporal coverage of

271 the observation data, the simulation period was from 16 October to 16 November 2019. Further

272 details on model settings can be found in Yang et al. (2022)

273   The empirical kinetic modeling approach (EKMA) is applied to investigate the sensitivity of

274 the production rate of RO$_2$ and OH to the variation of NO$_x$ and VOCs. The base case was simulated

275 based on the observation of average conditions. Sensitivity tests are performed by adjusting NO$_x$ or

276 VOCs by a ratio ranging from 0.1 to 2.0 without changing other parameters.

3. Results and discussion

3.1 Overview

279   Figure 1 shows the temporal profile of particle number size distribution (PNSD) and

280 condensation sink (CS) during the measurement (a), one-dimensional thermograms and T_{max}

281 measured by the FIGAERO-CIMS (b), bulk PM$_1$ chemical composition measured by the SP-AMS

282 and PM$_1$ concentration (c), deconvolved OA factors from PMF analysis (d), and wind speed and

283 direction (e). Note that all measurements started on 2 October. As shown in Fig. 1a, new particle

284 formation (NPF) events occurred frequently along with relatively low CS values during the

285 measurement period (44.4%, 20 out of 45 days). The T_{max} mainly varied in two temperature ranges,

286 80-95 °C and 110-120°C (Fig. 1b). The lower T_{max} was usually accompanied by high desorption

287 signals peaked at 80-95 °C (Fig. 1b), a higher fraction of LOOA (Fig. 1d), and an obvious wide

288 accumulation mode in PNSD (Fig. 1a).

289   The evening peak of hydrocarbon-like OA (HOA) and biomass burning OA (BBOA) was

290 related to local anthropogenic activities (e.g., biomass burning, cooking, and traffic, Fig. 2). The

291 less oxygenated OA (LOOA) and biomass burning SOA (BBSOA) showed afternoon peaks (Fig.

2), which could be attributed to secondary organic aerosol (SOA) formation through daytime photochemical reactions. LOOA showed a noticeable increase corresponding to the particle surface area (Fig. S8), while we did not observe such correlation for other SOA factors (MOOA and BBSOA). Furthermore, LOOA exhibited a stronger positive correlation with organic vapors measured by the FIGAERO-CIMS compared to other OA factors (Fig. S9). These results suggested that the daytime formation of LOOA was attributed to gas-particle partitioning. The O_x (O_x=O_3+NO_2) had a strong correlation with organic vapors in the afternoon (10:00-16:00 LT, Fig. S10), highlighting an important role of photochemical reaction on the formation of LOOA.

The high desorption signal at a lower temperature range suggested that the volatility of OA could be higher, which could be associated with the formation of LOOA. Coincidently, either NPF events or a higher fraction of LOOA could only be observed during the period prevalent with north wind direction (Fig. 1e), when the measurement site was affected by the pollutant from the city cluster around Guangzhou city. It indicates that the urban pollutants might promote particle formation and growth and daytime SOA formation by increasing oxidants and acting as precursor gases. Xiao et al. (2023) suggested that fresh urban emissions could enhance NPF, while NPF was suppressed in aged urban plumes. Shrivastava et al. (2019) found that urban emissions, including NO_x and oxidants, could significantly enhance the SOA formation in the Amazon rainforest. Three periods were classified based on the combination of wind direction and the analysis of backward trajectories to further investigate the impact of urban pollutants on this downwind site, which were long-range transport, urban air masses, and coastal air masses periods (Fig. S2 and Table. S2). The long-range transport period was related to long-range transport masses from northeast inland. The urban air masses period was mainly affected by regional urban air masses from the PRD region. The coastal air masses period was associated with air masses from the South China Sea and the northeast coast.

A significant daytime peak of LOOA (10.4 μg m^{-3}) was shown during the urban air masses period (Fig. 2c), while the enhancement of BBSOA was inapparent. It suggests that the contribution of gas-particle reactions on SOA formation was enhanced when the site was affected by urban plumes. The O_x concentration in the afternoon during the urban air masses period was higher than that during the long-range transport period (Fig. S11), which might be able to explain the significant enhancement of LOOA for the urban air masses period. These results imply that urban pollution

322 plumes could promote the formation of SOA in the downwind region by increasing the oxidant

323 concentration.

324 **3.2 The daytime formation of FIGAERO OA**

325 As aforementioned, the increase of LOOA was usually along with the significant desorption

326 signals measured by the FIGAERO-CIMS at a low temperature range (80-95°C), suggesting that

327 OA volatility could be higher. The average two-dimensional thermograms of all calibrated and semi-

328 quantified species and an example of a one-dimensional thermogram of levoglucosan can be found

329 in Fig. 3 a and b, respectively. According to Eqs. (1) and (2), we calculated the C^* value of all

330 calibrated and semi-quantified species based on their T_{max} and constructed volatility distribution as

331 volatility basis set (VBS, Fig. 3c). The T_{max} of each species is obtained based on their average

332 thermogram. These 12 VBS bins were classified into three groups(Donahue et al., 2012): semi-

333 volatile organic compounds (SVOC, $0.3 < C^* \leq 3 \times 10^2$ μg m^{-3}), less-volatile organic compounds

334 (LVOC, $3 \times 10^{-4} < C^* \leq 0.3$ μg m^{-3}), and extremely low-volatility organic compounds (ELVOC,

335 $C^* \leq 3 \times 10^{-4}$ μg m^{-3}). In general, most species measured by FIGAERO-CIMS fall into LVOC groups

336 (Fig. S12). Note that the decomposition of organic compounds was ignored in this method, which

337 could affect thermogram peaks in some cases and the measurement of low volatility compounds

338 (Wang and Hildebrandt Ruiz, 2018). Furthermore, the fraction of SVOC might be underestimated

339 owing to its high volatility, as a result fast evaporation could occur during the collection on the filter

340 and shifting from sampling mode to desorption mode.

341 During the urban air masses period, the FIGAERO-CIMS measured significant signals at a

342 desorption temperature range of SVOC and LVOC (Fig. S13) in the afternoon (12:00-16:00 LT),

343 indicating that the OA volatility could be higher. The SVOC+LVOC in the FIGAERO OA increased

344 from 5.2 μg m^{-3} (8:00 LT) to 16.29 μg m^{-3} (15:00 LT) during the urban air masses period (Fig. 4a),

345 which was coincident with an enhancement of LOOA (Fig. 2c). It suggested that daytime

346 enhancement of the SVOC+LVOC in the FIGAERO OA was closely related to the obvious LOOA

347 formation. The FIGAERO OA during the urban air masses period was systemically higher than that

348 during the long-range transport period, with a significantly higher concentration of LVOC group

349 (Fig. 4b), especially the portion with a volatility $log_{10}C^*$ of -1. Table 1 investigated the relationship

between SVOC+LVOC and six OA factors. The SVOC+LVOC in FIGAERO OA had a significant positive correlation (R=0.72-0.85) with the LOOA, especially during the urban air masses period (R=0.85, Fig. S14 and Table 1), suggesting that the LOOA formation was mainly responsible for the increase of OA volatility.

Interestingly, the high volatility organic vapors (SVOC+IVOC+VOC, $C^* > 0.3$ µg m^{-3}) dramatically increased in the afternoon during the urban air masses period, while we did not observe such phenomenon for low volatility (ELVOC+LVOC, $C^* \leq 0.3$ µg m^{-3}) organic vapors (Fig. 4c). The concentration of low volatility organic vapors in the afternoon (12:00-16:00 LT) did not show a significant difference (1.76 and 1.84 µg m^{-3}) between the long-range transport and urban air masses periods, indicating that the irreversible condensation of low volatility organic vapors could not fully explain the enhancement of LOOA during the urban air masses period (Wang et al., 2022). However, the high volatility organic vapors had a notably higher concentration (51.69 µg m^{-3}) during the urban air masses period than that (41.70 µg m^{-3}) during the long-range transport period. It implies that the significant enhancement of LOOA during the urban air masses period might be mainly attributed to the equilibrium partitioning of high volatility organic vapors, which could also increase the volatility of total OA.

Here we selected a typical day (2 November 2019) of the urban air masses period for further investigation. The measurement site was affected by the urban plume from the city cluster in the PRD region on this day (Fig. S15). A wide accumulation mode centered at about 180 nm in PNSD was observed, with a significant desorption signal measured by the FIGAERO-CIMS in the afternoon and weak north wind (Fig. S16). As shown in Fig. 5a, the desorption signals of organic compounds increased from 9:00 LT and reached their peak at 14:00 LT, suggesting a significant daytime SOA formation. The variation of OA volatility distribution and mean $C^*(\overline{C^*})$ is shown in Fig. 5b. The $\overline{C^*}$ shown an afternoon peak (0.021 µg m^{-3}) at 15:00 LT, suggesting a higher OA volatility in the afternoon. An evident enhancement of OA with a volatility $log_{10}C^*$ of -1 was observed in the afternoon, aligning with the formation of LOOA (Fig. 5c), which primarily contributes to higher OA volatility. Combined with the volatility distribution analysis in Fig. 4b, it indicated that the main components of LOOA have a volatility $log_{10}C^*$ of -1. Interestingly, the T_{max} value of the sum thermogram (Fig. 5a) increased from 81°C at 9:00 to 96°C at 17:00, implying that the OA volatility decreased during the daytime owing to the daytime aging processes. However,

380 the $\overline{C^*}$ value consistently increased from 6:00 LT until 15:00 LT and then began to decrease, which

381 was conflict with the increasing T_{max}. One possible reason is that species in the FIGAERO OA fell

382 into a specific T_{max} range (about 11°C) were categorized into different C^* bins by a factor of 10.

383 Thus, the slight variation of T_{max} might not affect the estimated volatility distribution of FIGAERO

384 OA. The other possible reason is that the volatility distribution of FIGAERO OA was estimated

385 based on the T_{max} value of calibrated and semi-quantified species, while the sum thermograms

386 contained all organic compounds containing C, H, and O atmos. There could be some organic

387 compounds formed through aging processes that were not included in the C^* estimation.

388 **3.3 The contribution of high volatility organic vapors to SOA formations**

389 In the previous section, we found that the significant enhancements in LOOA during the urban

390 air masses period might be attributed to the high volatility organic vapors through gas-particle

391 partitioning. The contribution of high volatility organic vapors to the OA concentration via

392 equilibrium partitioning can be estimated based on eq. (7). Our results show that the estimated

393 contribution of high volatility organic vapors (estimated OA$_{HVgas}$) was higher (peaked at about 1.17

394 µg m^{-3}) during the urban air masses period (Fig. 6a). Correspondingly, we observed an enhancement

395 in the measured concentration of these species in the particle-phase (measured OA$_{HVgas}$, peaked at

396 about 10.32 µg m^{-3}, Fig. 6b). This implies that the increase in high volatility organic vapors might

397 significantly contribute to the daytime SOA formation during the urban air masses period. However,

398 the estimated contribution was much lower than the measured value. It suggests that using the

399 equilibrium equation might not be able to fully explain the increase of LOOA contributed by the

400 high volatility organic vapors during the urban air masses period. Nie et al. (2022) indicated that the

401 estimation of OA contribution through the equilibrium equation can be easily disturbed by varied

402 meteorological processes, which would lead to uncertainties in the calculations.

403 Moreover, the gas-particle equilibrium theory assumes that particles are droplets and that the

404 high volatility species in the particle-phase could reach a reversible equilibrium with the gas-phase

405 concentration. However, some studies indicate that this assumption significantly overestimates the

406 volatility of these species in the particle-phase and underestimate the contribution of high volatility

407 organic vapors to the SOA concentration (Kolesar et al., 2015; Cappa and Wilson, 2011). This is

408   because particles might exist in a glassy state rather than a liquid state. It was consistent with the

409   difference of the volatility distribution of these species between the particle- and gas-phase (Fig.

410   7a). The volatility in the particle-phase was centered at a $log_{10}C^*$ of -1, while that in the gas-phase

411   showed a higher concentration of $log_{10}C^*$=6-8 μg m^{-3}, implying that the volatility of these

412   compounds in the particle-phase could lower than that in the gas-phase.

413   Another possible explanation is that the corresponding species in the particle-phase could be

414   the decomposition products of low volatility compounds, leading to a higher concentration than

415   expected. We further investigate the difference between the measured and estimated concentration

416   of different high volatility species (Fig. 7b). The measured concentration was systematically higher

417   than the estimated value. The higher measured concentration of $C_2H_2O_4I^-$ could be owing to the

418   decomposition of low volatility spices, as the desorption signal peaked at the ELVOC region (Fig.

419   7c). However, for higher molecular weight compounds, the corresponding T_{max} values were in the

420   LVOC region, suggesting that these species might not be the decomposition products. This implies

421   that the decomposition products might play a minor effect in the difference between the measured

422   and estimated concentration.

423   Taken together, these results suggest the increase in high volatility organic vapors could

424   promote the daytime enhancement of SOA during urban air masses period. However, this

425   contribution might be underestimated using gas-particle equilibrium theory, since the volatility of

426   organic aerosol may differ significantly from the volatility determined by the equilibrium theory.

427   **3.4 Enhancement of SOA formation by urban pollutants**

428   As aforementioned, the significant enhancement of high volatility organic vapors were

429   observed during the urban air masses period. Figure 8 compares the difference of organic vapors in

430   the carbon oxidation state ($\overline{OS_C}$) in the afternoon (12:00-16:00 LT) between the long-range transport

431   and urban air masses periods. A higher concentration of organic vapors with a low $\overline{OS_C}$ ($\overline{OS_C} \leq 0$)

432   was observed during the urban air masses period, while this trend became to overturn for high $\overline{OS_C}$

433   ($\overline{OS_C}$>0) organic vapors. It suggests that the oxidation degree of organic vapors was lower during

434   the urban air masses period, even though the O_x concentration was higher (Fig. S11). This trend was

435   more significant for carbon number between 2 and 5, indicating a higher concentration of small

436   molecules with low $\overline{OS_C}$ during urban air masses period. The $\overline{OS_C}$ of major C_5 compounds was

437   about -1.33, which was mainly contributed by $C_5H_8NOI^-$, highlighting the role of NO_x chemistry.

438   The oxygenated organic vapors production rates depend on oxidant and precursor concentration,

439   and the mechanism of significant enhancement of high volatility organic vapors remain unclear. We

440   speculated that it could be partly attributed to the elevated NO_x concentration in the afternoon during

441   the urban air masses period (Fig. S17). NO_x was found to have a detrimental effect on the production

442   of highly oxidized products, and thus the formation of low volatility vapors (Rissanen, 2018), which

443   might be responsible for the smooth increase of low volatility organic vapors. Previous studies found

444   that the increase of NO_x could lead to higher OH production, which would offset decreases in the

445   autoxidation efficiency and further result in enhanced SOA formation (Liu et al., 2021; Pye et al.,

446   2019). During the urban air masses period, both low volatility and high volatility CHON compounds

447   increased in the afternoon, implying the effect of NO_x on the photochemical reactions (Fig. S18 a

448   and b). That was further evidenced by the higher fraction of CHON compounds in the FIGAERO

449   OA (Fig. S18f). This result was consistent with Schwantes et al. (2019), who reported that low

450   volatility organic nitrates might have a significant contribution to SOA under high NO_x conditions.

451   Interestingly, in contrast with the higher fraction of low volatility CHON compounds in the

452   afternoon, the fraction of high volatility CHON compounds was lower at the same time (Fig. S18 d

453   and e), indicating that the effect of high NO_x concentration on photochemical oxidation goes beyond

454   the formation of CHON compounds for high volatility species.

455   To further understand how the urban plumes affect the SOA formation, we used an observation-

456   constrained box model to simulate the production rate of organic peroxy radicals (RO_2) and OH

457   with different NO_x and VOCs concentrations (Fig. 9). The detailed description of the box model is

458   described in Sect. 2.3.4. In general, the production rates of OH (P(OH)) were close to the transition

459   regime during three selected periods (Fig. 9a), where the P(OH) is sensitive to both VOCs and NO_x

460   variation. Further, the P(OH) tended to be in the NO_x-limited regime during the coastal air masses

461   period. The emission of NO_x might enhance the atmospheric oxidation capacity, consistent with the

462   results from other observations (Shrivastava et al., 2019; Pye et al., 2019). Interestingly, the

463   sensitivity regime of P(OH) changed to the VOCs-limited during the urban air masses period,

464   suggesting that the production of OH would be suppressed with continued increases in NO_x. During

465   the urban air masses period, the concentration of NO_x and VOCs was noticeably increased compared

466   to the coastal air masses period, leading to a significant increase of P(OH).

467   Recent studies show that autooxidation of RO_2 can result in highly oxygenated molecules

468   (O:C≥0.7) and promote SOA formation(Pye et al., 2019; Pye et al., 2015). In general, the production

469   rate of RO_2 (P(RO_2)) was in the VOCs-limited regime during three selected periods (Fig. 9b), where

470   the P(RO_2) increased with the increase of VOCs. It suggests that the production of RO_2 was

471   suppressed with the increase in NO_x. During the urban air masses period, the concentration of VOCs

472   was noticeably increased compared to the coastal air masses period, leading to a significant increase

473   of P(RO_2). The model results indicate that urban pollutants, including NO_x and VOCs, could

474   enhance the oxidizing capacity, while the increase of VOCs was mainly responsible for significant

475   daytime SOA formation.

4. Conclusions

477   In this study, we demonstrated that daytime SOA formation could be enhanced when the rural

478   site was affected by the pollutant from the city region, which could be partly attributed to the high

479   concentration of oxidant in the urban pollution. A higher volatility of OA was observed during the

480   urban air masses period, which was mainly contributed by the component with a volatility $log_{10}C^*$

481   of -1. The significant increase of SVOC+LVOC in FIGAERO OA in the afternoon was associated

482   with enhanced LOOA formation. Similar to other measurements, the daytime formation of LOOA

483   was mainly through gas-to-particle partitioning of organic vapors, supported by a significant

484   positive relationship between the LOOA and organic vapors. We observed a dramatic increase in

485   the high volatility organic vapors in the afternoon during the urban air masses period, while low

486   volatility organic vapors did not exhibit a similar growth trend. It indicated that the rapid increase

487   of LOOA during the urban air masses period was mainly contributed by the gas-particle partitioning

488   of high volatility organic vapors. However, this contribution was underestimated using equilibrium

489   theory, since the volatility of high organic vapors in the particle phase was significantly lower than

490   that in the gas-phase.

491   The high NO_x might also suppress the formation of highly oxidized products. Thus, the

492   elevated NO_x in the urban plume might be able to explain the smooth increase in low volatility

493   organic vapors and a higher concentration of organic vapors with a low $\overline{OS_C}$. Box model simulation

494 showed that the P(OH) were close to the transition regime during three selected periods, indicating
495 that the elevated NO_x and VOCs in urban plumes can increase the oxidizing capacity. However, the
496 P(RO_2) was in the VOCs-limited regime, suggesting that the increase in VOCs was mainly
497 responsible for the daytime enhancement of SOA. Further investigations on the effect of urban
498 pollutants on SOA formation on the regional scale are still needed for formulating air pollution
499 control strategies.

500

501 *Data availability.* Data from the measurements are available at
502 https://doi.org/10.6084/m9.figshare.25376059.

503

504 *Supplement.* The supplement related to this article is available online at xxx.

505

506 *Author contributions.* **MC, YC, and BY** designed the research. **MC, YC, BY, SH, EZ, ZW, YL,**
507 **TL, WH, WC, QS, WL, YP, BL, QS, and JZ** performed the measurements. **MC, YC, BY, SH,**
508 **EZ, SY, ZW, YL, TL, WH, WC, QS, WL, YP, BL, QS, and JZ** analyzed the data. **MC, YC, and**
509 **BY** wrote the paper with contributions from all co-authors.

510

511 *Competing interests.* The authors declare that they have no conflict of interest.

512

532

References

Apte, J. S., Brauer, M., Cohen, A. J., Ezzati, M., and Pope, C. A., III: Ambient PM2.5 Reduces Global and Regional Life Expectancy, Environmental Science & Technology Letters, 5, 546-551, 10.1021/acs.estlett.8b00360, 2018.

Arias, P., Bellouin, N., Coppola, E., Jones, R., Krinner, G., Marotzke, J., Naik, V., Palmer, M., Plattner, G.-K., Rogelj, J., Rojas, M., Sillmann, J., Storelvmo, T., Thorne, P., Trewin, B., Rao, K., Adhikary, B., Allan, R., Armour, K., and Zickfeld, K.: IPCC AR6 WGI Technical Summary, in, In Press.

Baublitz, C. B., Fiore, A. M., Ludwig, S. M., Nicely, J. M., Wolfe, G. M., Murray, L. T., Commane, R., Prather, M. J., Anderson, D. C., Correa, G., Duncan, B. N., Follette-Cook, M., Westervelt, D. M., Bourgeois, I., Brune, W. H., Bui, T. P., DiGangi, J. P., Diskin, G. S., Hall, S. R., McKain, K., Miller, D. O., Peischl, J., Thames, A. B., Thompson, C. R., Ullmann, K., and Wofsy, S. C.: An observation-based, reduced-form model for oxidation in the remote marine troposphere, Proceedings of the National Academy of Sciences, 120, e2209735120, 10.1073/pnas.2209735120, 2023.

Bertrand, A., Stefenelli, G., Jen, C. N., Pieber, S. M., Bruns, E. A., Ni, H., Temime-Roussel, B., Slowik, J. G., Goldstein, A. H., El Haddad, I., Baltensperger, U., Prévôt, A. S. H., Wortham, H., and Marchand, N.: Evolution of the chemical fingerprint of biomass burning organic aerosol during aging, Atmos. Chem. Phys., 18, 7607-7624, 10.5194/acp-18-7607-2018, 2018.

Bianchi, F., Kurtén, T., Riva, M., Mohr, C., Rissanen, M. P., Roldin, P., Berndt, T., Crounse, J. D., Wennberg, P. O., Mentel, T. F., Wildt, J., Junninen, H., Jokinen, T., Kulmala, M., Worsnop, D. R., Thornton, J. A., Donahue, N., Kjaergaard, H. G., and Ehn, M.: Highly Oxygenated Organic Molecules (HOM) from Gas-Phase Autoxidation Involving Peroxy Radicals: A Key Contributor to Atmospheric Aerosol, Chemical Reviews, 119, 3472-3509, 10.1021/acs.chemrev.8b00395, 2019.

Buchholz, A., Ylisirniö, A., Huang, W., Mohr, C., Canagaratna, M., Worsnop, D. R., Schobesberger, S., and Virtanen, A.: Deconvolution of FIGAERO–CIMS thermal desorption profiles using positive matrix factorisation to identify chemical and physical processes during particle evaporation, Atmos. Chem. Phys., 20, 7693-7716, 10.5194/acp-20-7693-2020, 2020.

Cai, M., Liang, B., Sun, Q., Liu, L., Yuan, B., Shao, M., Huang, S., Peng, Y., Wang, Z., Tan, H., Li, F., Xu, H., Chen, D., and Zhao, J.: The important roles of surface tension and growth rate in the contribution of new particle formation (NPF) to cloud condensation nuclei (CCN) number concentration: evidence from field measurements in southern China, Atmos. Chem. Phys., 21, 8575-8592, 10.5194/acp-21-8575-2021, 2021.

Cai, M., Huang, S., Liang, B., Sun, Q., Liu, L., Yuan, B., Shao, M., Hu, W., Chen, W., Song, Q., Li, W., Peng, Y., Wang, Z., Chen, D., Tan, H., Xu, H., Li, F., Deng, X., Deng, T., Sun, J., and Zhao, J.: Measurement report: Distinct size dependence and diurnal variation in organic aerosol hygroscopicity, volatility, and cloud condensation nuclei activity at a rural site in the Pearl River Delta (PRD) region, China, Atmos. Chem. Phys., 22, 8117-8136, 10.5194/acp-22-8117-2022, 2022.

Cai, Y., Ye, C., Chen, W., Hu, W., Song, W., Peng, Y., Huang, S., Qi, J., Wang, S., Wang, C., Wu, C., Wang, Z., Wang, B., Huang, X., He, L., Gligorovski, S., Yuan, B., Shao, M., and Wang, X.: The important contribution of secondary formation and biomass burning to oxidized organic nitrogen (OON) in a polluted urban area: insights from in situ measurements of a chemical

575 ionization mass spectrometer (CIMS), Atmos. Chem. Phys., 23, 8855-8877, 10.5194/acp-23-8855-
576 2023, 2023.

577 Cappa, C. D. and Wilson, K. R.: Evolution of organic aerosol mass spectra upon heating:
578 implications for OA phase and partitioning behavior, Atmos. Chem. Phys., 11, 1895-1911,
579 10.5194/acp-11-1895-2011, 2011.

580 Chen, Y., Takeuchi, M., Nah, T., Xu, L., Canagaratna, M. R., Stark, H., Baumann, K., Canonaco,
581 F., Prévôt, A. S. H., Huey, L. G., Weber, R. J., and Ng, N. L.: Chemical characterization of secondary
582 organic aerosol at a rural site in the southeastern US: insights from simultaneous high-resolution
583 time-of-flight aerosol mass spectrometer (HR-ToF-AMS) and FIGAERO chemical ionization mass
584 spectrometer (CIMS) measurements, Atmos. Chem. Phys., 20, 8421-8440, 10.5194/acp-20-8421-
585 2020, 2020.

586 D'Ambro, E. L., Møller, K. H., Lopez-Hilfiker, F. D., Schobesberger, S., Liu, J., Shilling, J. E.,
587 Lee, B. H., Kjaergaard, H. G., and Thornton, J. A.: Isomerization of Second-Generation Isoprene
588 Peroxy Radicals: Epoxide Formation and Implications for Secondary Organic Aerosol Yields,
589 Environmental Science & Technology, 51, 4978-4987, 10.1021/acs.est.7b00460, 2017.

590 de Sá, S. S., Palm, B. B., Campuzano-Jost, P., Day, D. A., Hu, W., Isaacman-VanWertz, G., Yee,
591 L. D., Brito, J., Carbone, S., Ribeiro, I. O., Cirino, G. G., Liu, Y., Thalman, R., Sedlacek, A., Funk,
592 A., Schumacher, C., Shilling, J. E., Schneider, J., Artaxo, P., Goldstein, A. H., Souza, R. A. F., Wang,
593 J., McKinney, K. A., Barbosa, H., Alexander, M. L., Jimenez, J. L., and Martin, S. T.: Urban
594 influence on the concentration and composition of submicron particulate matter in central Amazonia,
595 Atmos. Chem. Phys., 18, 12185-12206, 10.5194/acp-18-12185-2018, 2018.

596 Donahue, N. M., Epstein, S. A., Pandis, S. N., and Robinson, A. L.: A two-dimensional
597 volatility basis set: 1. organic-aerosol mixing thermodynamics, Atmos. Chem. Phys., 11, 3303-3318,
598 10.5194/acp-11-3303-2011, 2011.

599 Donahue, N. M., Kroll, J. H., Pandis, S. N., and Robinson, A. L.: A two-dimensional volatility
600 basis set – Part 2: Diagnostics of organic-aerosol evolution, Atmos. Chem. Phys., 12, 615-634,
601 10.5194/acp-12-615-2012, 2012.

602 Dong, H. B., Zeng, L. M., Hu, M., Wu, Y. S., Zhang, Y. H., Slanina, J., Zheng, M., Wang, Z.
603 F., and Jansen, R.: Technical Note: The application of an improved gas and aerosol collector for
604 ambient air pollutants in China, Atmos. Chem. Phys., 12, 10519-10533, 10.5194/acp-12-10519-
605 2012, 2012.

606 Ervens, B., Turpin, B. J., and Weber, R. J.: Secondary organic aerosol formation in cloud
607 droplets and aqueous particles (aqSOA): a review of laboratory, field and model studies, Atmos.
608 Chem. Phys., 11, 11069-11102, 10.5194/acp-11-11069-2011, 2011.

609 Fry, J. L., Brown, S. S., Middlebrook, A. M., Edwards, P. M., Campuzano-Jost, P., Day, D. A.,
610 Jimenez, J. L., Allen, H. M., Ryerson, T. B., Pollack, I., Graus, M., Warneke, C., de Gouw, J. A.,
611 Brock, C. A., Gilman, J., Lerner, B. M., Dubé, W. P., Liao, J., and Welti, A.: Secondary organic
612 aerosol (SOA) yields from NO3 radical + isoprene based on nighttime aircraft power plant plume
613 transects, Atmos. Chem. Phys., 18, 11663-11682, 10.5194/acp-18-11663-2018, 2018.

614 Hallquist, M., Wenger, J. C., Baltensperger, U., Rudich, Y., Simpson, D., Claeys, M., Dommen,
615 J., Donahue, N. M., George, C., Goldstein, A. H., Hamilton, J. F., Herrmann, H., Hoffmann, T.,
616 Iinuma, Y., Jang, M., Jenkin, M. E., Jimenez, J. L., Kiendler-Scharr, A., Maenhaut, W., McFiggans,
617 G., Mentel, T. F., Monod, A., Prévôt, A. S. H., Seinfeld, J. H., Surratt, J. D., Szmigielski, R., and
618 Wildt, J.: The formation, properties and impact of secondary organic aerosol: current and emerging

issues, Atmos. Chem. Phys., 9, 5155-5236, 10.5194/acp-9-5155-2009, 2009.

Hodzic, A., Jimenez, J. L., Madronich, S., Canagaratna, M. R., DeCarlo, P. F., Kleinman, L., and Fast, J.: Modeling organic aerosols in a megacity: potential contribution of semi-volatile and intermediate volatility primary organic compounds to secondary organic aerosol formation, Atmos. Chem. Phys., 10, 5491-5514, 10.5194/acp-10-5491-2010, 2010.

Huang, R.-J., Zhang, Y., Bozzetti, C., Ho, K.-F., Cao, J.-J., Han, Y., Daellenbach, K. R., Slowik, J. G., Platt, S. M., Canonaco, F., Zotter, P., Wolf, R., Pieber, S. M., Bruns, E. A., Crippa, M., Ciarelli, G., Piazzalunga, A., Schwikowski, M., Abbaszade, G., Schnelle-Kreis, J., Zimmermann, R., An, Z., Szidat, S., Baltensperger, U., Haddad, I. E., and Prevot, A. S. H.: High secondary aerosol contribution to particulate pollution during haze events in China, Nature, 514, 218–222, 10.1038/nature13774
http://www.nature.com/nature/journal/vaop/ncurrent/abs/nature13774.html#supplementary-information, 2014.

Huang, W., Saathoff, H., Pajunoja, A., Shen, X., Naumann, K. H., Wagner, R., Virtanen, A., Leisner, T., and Mohr, C.: α-Pinene secondary organic aerosol at low temperature: chemical composition and implications for particle viscosity, Atmos. Chem. Phys., 18, 2883-2898, 10.5194/acp-18-2883-2018, 2018.

Iyer, S., Lopez-Hilfiker, F., Lee, B. H., Thornton, J. A., and Kurtén, T.: Modeling the Detection of Organic and Inorganic Compounds Using Iodide-Based Chemical Ionization, The Journal of Physical Chemistry A, 120, 576-587, 10.1021/acs.jpca.5b09837, 2016.

Kolesar, K. R., Li, Z., Wilson, K. R., and Cappa, C. D.: Heating-Induced Evaporation of Nine Different Secondary Organic Aerosol Types, Environmental Science & Technology, 49, 12242-12252, 10.1021/acs.est.5b03038, 2015.

Kuang, Y., Huang, S., Xue, B., Luo, B., Song, Q., Chen, W., Hu, W., Li, W., Zhao, P., Cai, M., Peng, Y., Qi, J., Li, T., Wang, S., Chen, D., Yue, D., Yuan, B., and Shao, M.: Contrasting effects of secondary organic aerosol formations on organic aerosol hygroscopicity, Atmos. Chem. Phys., 21, 10375-10391, 10.5194/acp-21-10375-2021, 2021.

Lanzafame, G. M., Srivastava, D., Favez, O., Bandowe, B. A. M., Shahpoury, P., Lammel, G., Bonnaire, N., Alleman, L. Y., Couvidat, F., Bessagnet, B., and Albinet, A.: One-year measurements of secondary organic aerosol (SOA) markers in the Paris region (France): Concentrations, gas/particle partitioning and SOA source apportionment, Science of The Total Environment, 757, 143921, https://doi.org/10.1016/j.scitotenv.2020.143921, 2021.

Le Breton, M., Wang, Y., Hallquist, Å. M., Pathak, R. K., Zheng, J., Yang, Y., Shang, D., Glasius, M., Bannan, T. J., Liu, Q., Chan, C. K., Percival, C. J., Zhu, W., Lou, S., Topping, D., Wang, Y., Yu, J., Lu, K., Guo, S., Hu, M., and Hallquist, M.: Online gas- and particle-phase measurements of organosulfates, organosulfonates and nitrooxy organosulfates in Beijing utilizing a FIGAERO ToF-CIMS, Atmos. Chem. Phys., 18, 10355-10371, 10.5194/acp-18-10355-2018, 2018.

Lee, B.-H., Kostenidou, E., Hildebrandt, L., Riipinen, I., Engelhart, G., Mohr, C., DeCarlo, P., Mihalopoulos, N., Prevot, A., Baltensperger, U. J. A. C., and Physics: Measurement of the ambient organic aerosol volatility distribution: application during the Finokalia Aerosol Measurement Experiment (FAME-2008), 10, 12149-12160, 2010.

Liu, Y., Seco, R., Kim, S., Guenther, A. B., Goldstein, A. H., Keutsch, F. N., Springston, S. R., Watson, T. B., Artaxo, P., Souza, R. A. F., McKinney, K. A., and Martin, S. T.: Isoprene photo-oxidation products quantify the effect of pollution on hydroxyl radicals over Amazonia, Science

Advances, 4, eaar2547, doi:10.1126/sciadv.aar2547, 2018.

Liu, Y., Nie, W., Li, Y., Ge, D., Liu, C., Xu, Z., Chen, L., Wang, T., Wang, L., Sun, P., Qi, X., Wang, J., Xu, Z., Yuan, J., Yan, C., Zhang, Y., Huang, D., Wang, Z., Donahue, N. M., Worsnop, D., Chi, X., Ehn, M., and Ding, A.: Formation of condensable organic vapors from anthropogenic and biogenic volatile organic compounds (VOCs) is strongly perturbed by NOx in eastern China, Atmos. Chem. Phys., 21, 14789-14814, 10.5194/acp-21-14789-2021, 2021.

Lopez-Hilfiker, F. D., Iyer, S., Mohr, C., Lee, B. H., D'Ambro, E. L., Kurtén, T., and Thornton, J. A.: Constraining the sensitivity of iodide adduct chemical ionization mass spectrometry to multifunctional organic molecules using the collision limit and thermodynamic stability of iodide ion adducts, Atmos. Meas. Tech., 9, 1505-1512, 10.5194/amt-9-1505-2016, 2016.

Lopez-Hilfiker, F. D., Mohr, C., Ehn, M., Rubach, F., Kleist, E., Wildt, J., Mentel, T. F., Lutz, A., Hallquist, M., Worsnop, D., and Thornton, J. A.: A novel method for online analysis of gas and particle composition: description and evaluation of a Filter Inlet for Gases and AEROsols (FIGAERO), Atmos. Meas. Tech., 7, 983-1001, 10.5194/amt-7-983-2014, 2014.

Luo, B., Kuang, Y., Huang, S., Song, Q., Hu, W., Li, W., Peng, Y., Chen, D., Yue, D., Yuan, B., and Shao, M.: Parameterizations of size distribution and refractive index of biomass burning organic aerosol with black carbon content, Atmos. Chem. Phys., 22, 12401-12415, 10.5194/acp-22-12401-2022, 2022.

Masoud, C. G., Li, Y., Wang, D. S., Katz, E. F., DeCarlo, P. F., Farmer, D. K., Vance, M. E., Shiraiwa, M., and Hildebrandt Ruiz, L.: Molecular composition and gas-particle partitioning of indoor cooking aerosol: Insights from a FIGAERO-CIMS and kinetic aerosol modeling, Aerosol Science and Technology, 56, 1156-1173, 10.1080/02786826.2022.2133593, 2022.

Mohr, C., Thornton, J. A., Heitto, A., Lopez-Hilfiker, F. D., Lutz, A., Riipinen, I., Hong, J., Donahue, N. M., Hallquist, M., and Petäjä, T. J. N. c.: Molecular identification of organic vapors driving atmospheric nanoparticle growth, 10, 1-7, 2019.

Mutzel, A., Poulain, L., Berndt, T., Iinuma, Y., Rodigast, M., Böge, O., Richters, S., Spindler, G., Sipilä, M., Jokinen, T., Kulmala, M., and Herrmann, H.: Highly Oxidized Multifunctional Organic Compounds Observed in Tropospheric Particles: A Field and Laboratory Study, Environmental Science & Technology, 49, 7754-7761, 10.1021/acs.est.5b00885, 2015.

Ng, N. L., Canagaratna, M. R., Jimenez, J. L., Zhang, Q., Ulbrich, I. M., and Worsnop, D. R.: Real-Time Methods for Estimating Organic Component Mass Concentrations from Aerosol Mass Spectrometer Data, Environmental Science & Technology, 45, 910-916, 10.1021/es102951k, 2011.

Nie, W., Yan, C., Huang, D. D., Wang, Z., Liu, Y., Qiao, X., Guo, Y., Tian, L., Zheng, P., Xu, Z., Li, Y., Xu, Z., Qi, X., Sun, P., Wang, J., Zheng, F., Li, X., Yin, R., Dallenbach, K. R., Bianchi, F., Petäjä, T., Zhang, Y., Wang, M., Schervish, M., Wang, S., Qiao, L., Wang, Q., Zhou, M., Wang, H., Yu, C., Yao, D., Guo, H., Ye, P., Lee, S., Li, Y. J., Liu, Y., Chi, X., Kerminen, V.-M., Ehn, M., Donahue, N. M., Wang, T., Huang, C., Kulmala, M., Worsnop, D., Jiang, J., and Ding, A.: Secondary organic aerosol formed by condensing anthropogenic vapours over China's megacities, Nature Geoscience, 10.1038/s41561-022-00922-5, 2022.

Peng, Z., Lee-Taylor, J., Orlando, J. J., Tyndall, G. S., and Jimenez, J. L.: Organic peroxy radical chemistry in oxidation flow reactors and environmental chambers and their atmospheric relevance, Atmos. Chem. Phys., 19, 813-834, 10.5194/acp-19-813-2019, 2019.

Philippin, S., Wiedensohler, A., and Stratmann, F.: Measurements of non-volatile fractions of pollution aerosols with an eight-tube volatility tandem differential mobility analyzer (VTDMA-8),

707 Journal of Aerosol Science, 35, 185-203, http://dx.doi.org/10.1016/j.jaerosci.2003.07.004, 2004.

708 Praske, E., Otkjær, R. V., Crounse, J. D., Hethcox, J. C., Stoltz, B. M., Kjaergaard, H. G., and
709 Wennberg, P. O.: Atmospheric autoxidation is increasingly important in urban and suburban North
710 America, Proceedings of the National Academy of Sciences, 115, 64-69, 10.1073/pnas.1715540115,
711 2018.

712 Pye, H. O. T., Luecken, D. J., Xu, L., Boyd, C. M., Ng, N. L., Baker, K. R., Ayres, B. R., Bash,
713 J. O., Baumann, K., Carter, W. P. L., Edgerton, E., Fry, J. L., Hutzell, W. T., Schwede, D. B., and
714 Shepson, P. B.: Modeling the Current and Future Roles of Particulate Organic Nitrates in the
715 Southeastern United States, Environmental Science & Technology, 49, 14195-14203,
716 10.1021/acs.est.5b03738, 2015.

717 Pye, H. O. T., D'Ambro, E. L., Lee, B. H., Schobesberger, S., Takeuchi, M., Zhao, Y., Lopez-
718 Hilfiker, F., Liu, J., Shilling, J. E., Xing, J., Mathur, R., Middlebrook, A. M., Liao, J., Welti, A.,
719 Graus, M., Warneke, C., de Gouw, J. A., Holloway, J. S., Ryerson, T. B., Pollack, I. B., and Thornton,
720 J. A.: Anthropogenic enhancements to production of highly oxygenated molecules from
721 autoxidation, Proceedings of the National Academy of Sciences, 116, 6641-6646,
722 10.1073/pnas.1810774116, 2019.

723 Ren, S., Yao, L., Wang, Y., Yang, G., Liu, Y., Li, Y., Lu, Y., Wang, L., and Wang, L.: Volatility
724 parameterization of ambient organic aerosols at a rural site of the North China Plain, Atmos. Chem.
725 Phys., 22, 9283-9297, 10.5194/acp-22-9283-2022, 2022.

726 Rissanen, M. P.: NO2 Suppression of Autoxidation–Inhibition of Gas-Phase Highly Oxidized
727 Dimer Product Formation, ACS Earth and Space Chemistry, 2, 1211-1219,
728 10.1021/acsearthspacechem.8b00123, 2018.

729 Saha, P. K., Khlystov, A., Yahya, K., Zhang, Y., Xu, L., Ng, N. L., Grieshop, A. P. J. A. C., and
730 Physics: Quantifying the volatility of organic aerosol in the southeastern US, 17, 501-520, 2017.

731 Salvador, C. M. G., Tang, R., Priestley, M., Li, L., Tsiligiannis, E., Le Breton, M., Zhu, W.,
732 Zeng, L., Wang, H., Yu, Y., Hu, M., Guo, S., and Hallquist, M.: Ambient nitro-aromatic compounds
733 – biomass burning versus secondary formation in rural China, Atmos. Chem. Phys., 21, 1389-1406,
734 10.5194/acp-21-1389-2021, 2021.

735 Schwantes, R. H., Charan, S. M., Bates, K. H., Huang, Y., Nguyen, T. B., Mai, H., Kong, W.,
736 Flagan, R. C., and Seinfeld, J. H.: Low-volatility compounds contribute significantly to isoprene
737 secondary organic aerosol (SOA) under high-NOx conditions, Atmos. Chem. Phys., 19, 7255-7278,
738 10.5194/acp-19-7255-2019, 2019.

739 Shrivastava, M., Andreae, M. O., Artaxo, P., Barbosa, H. M. J., Berg, L. K., Brito, J., Ching, J.,
740 Easter, R. C., Fan, J., Fast, J. D., Feng, Z., Fuentes, J. D., Glasius, M., Goldstein, A. H., Alves, E.
741 G., Gomes, H., Gu, D., Guenther, A., Jathar, S. H., Kim, S., Liu, Y., Lou, S., Martin, S. T., McNeill,
742 V. F., Medeiros, A., de Sá, S. S., Shilling, J. E., Springston, S. R., Souza, R. A. F., Thornton, J. A.,
743 Isaacman-VanWertz, G., Yee, L. D., Ynoue, R., Zaveri, R. A., Zelenyuk, A., and Zhao, C.: Urban
744 pollution greatly enhances formation of natural aerosols over the Amazon rainforest, Nature
745 Communications, 10, 1046, 10.1038/s41467-019-08909-4, 2019.

746 Wang, D. S. and Hildebrandt Ruiz, L.: Chlorine-initiated oxidation of n-alkanes under high-
747 NOx conditions: insights into secondary organic aerosol composition and volatility using a
748 FIGAERO–CIMS, Atmos. Chem. Phys., 18, 15535-15553, 10.5194/acp-18-15535-2018, 2018.

749 Wang, Y., Zhang, Y., Hao, J., and Luo, M.: Seasonal and spatial variability of surface ozone
750 over China: contributions from background and domestic pollution, Atmos. Chem. Phys., 11, 3511-

751   3525, 10.5194/acp-11-3511-2011, 2011.

752   Wang, Y., Hu, M., Wang, Y., Zheng, J., Shang, D., Yang, Y., Liu, Y., Li, X., Tang, R., Zhu, W.,
753   Du, Z., Wu, Y., Guo, S., Wu, Z., Lou, S., Hallquist, M., and Yu, J. Z.: The formation of nitro-aromatic
754   compounds under high NOx and anthropogenic VOC conditions in urban Beijing, China, Atmos.
755   Chem. Phys., 19, 7649-7665, 10.5194/acp-19-7649-2019, 2019.

756   Wang, Y., Clusius, P., Yan, C., Dällenbach, K., Yin, R., Wang, M., He, X.-C., Chu, B., Lu, Y.,
757   Dada, L., Kangasluoma, J., Rantala, P., Deng, C., Lin, Z., Wang, W., Yao, L., Fan, X., Du, W., Cai,
758   J., Heikkinen, L., Tham, Y. J., Zha, Q., Ling, Z., Junninen, H., Petäjä, T., Ge, M., Wang, Y., He, H.,
759   Worsnop, D. R., Kerminen, V.-M., Bianchi, F., Wang, L., Jiang, J., Liu, Y., Boy, M., Ehn, M.,
760   Donahue, N. M., and Kulmala, M.: Molecular Composition of Oxygenated Organic Molecules and
761   Their Contributions to Organic Aerosol in Beijing, Environmental Science & Technology, 56, 770-
762   778, 10.1021/acs.est.1c05191, 2022.

763   Wolfe, G. M., Marvin, M. R., Roberts, S. J., Travis, K. R., and Liao, J.: The Framework for 0-
764   D Atmospheric Modeling (F0AM) v3.1, Geosci. Model Dev., 9, 3309-3319, 10.5194/gmd-9-3309-
765   2016, 2016.

766   Xiao, Q., Zhang, J., Wang, Y., Ziemba, L. D., Crosbie, E., Winstead, E. L., Robinson, C. E.,
767   DiGangi, J. P., Diskin, G. S., Reid, J. S., Schmidt, K. S., Sorooshian, A., Hilario, M. R. A., Woods,
768   S., Lawson, P., Stamnes, S. A., and Wang, J.: New particle formation in the tropical free troposphere
769   during CAMP2Ex: statistics and impact of emission sources, convective activity, and synoptic
770   conditions, Atmos. Chem. Phys., 23, 9853-9871, 10.5194/acp-23-9853-2023, 2023.

771   Yang, S., Yuan, B., Peng, Y., Huang, S., Chen, W., Hu, W., Pei, C., Zhou, J., Parrish, D. D.,
772   Wang, W., He, X., Cheng, C., Li, X. B., Yang, X., Song, Y., Wang, H., Qi, J., Wang, B., Wang, C.,
773   Wang, C., Wang, Z., Li, T., Zheng, E., Wang, S., Wu, C., Cai, M., Ye, C., Song, W., Cheng, P., Chen,
774   D., Wang, X., Zhang, Z., Wang, X., Zheng, J., and Shao, M.: The formation and mitigation of nitrate
775   pollution: comparison between urban and suburban environments, Atmos. Chem. Phys., 22, 4539-
776   4556, 10.5194/acp-22-4539-2022, 2022.

777   Ye, C., Yuan, B., Lin, Y., Wang, Z., Hu, W., Li, T., Chen, W., Wu, C., Wang, C., Huang, S., Qi,
778   J., Wang, B., Wang, C., Song, W., Wang, X., Zheng, E., Krechmer, J. E., Ye, P., Zhang, Z., Wang,
779   X., Worsnop, D. R., and Shao, M.: Chemical characterization of oxygenated organic compounds in
780   the gas phase and particle phase using iodide CIMS with FIGAERO in urban air, Atmos. Chem.
781   Phys., 21, 8455-8478, 10.5194/acp-21-8455-2021, 2021.

782   Ylisirniö, A., Buchholz, A., Mohr, C., Li, Z., Barreira, L., Lambe, A., Faiola, C., Kari, E., Yli-
783   Juuti, T., Nizkorodov, S. A., Worsnop, D. R., Virtanen, A., and Schobesberger, S.: Composition and
784   volatility of secondary organic aerosol (SOA) formed from oxidation of real tree emissions
785   compared to simplified volatile organic compound (VOC) systems, Atmos. Chem. Phys., 20, 5629-
786   5644, 10.5194/acp-20-5629-2020, 2020.

787   Zhang, Q., Zheng, Y., Tong, D., Shao, M., Wang, S., Zhang, Y., Xu, X., Wang, J., He, H., Liu,
788   W., Ding, Y., Lei, Y., Li, J., Wang, Z., Zhang, X., Wang, Y., Cheng, J., Liu, Y., Shi, Q., Yan, L., Geng,
789   G., Hong, C., Li, M., Liu, F., Zheng, B., Cao, J., Ding, A., Gao, J., Fu, Q., Huo, J., Liu, B., Liu, Z.,
790   Yang, F., He, K., and Hao, J.: Drivers of improved PM2.5 air quality in China from 2013 to 2017,
791   Proceedings of the National Academy of Sciences, 116, 24463-24469, 10.1073/pnas.1907956116,
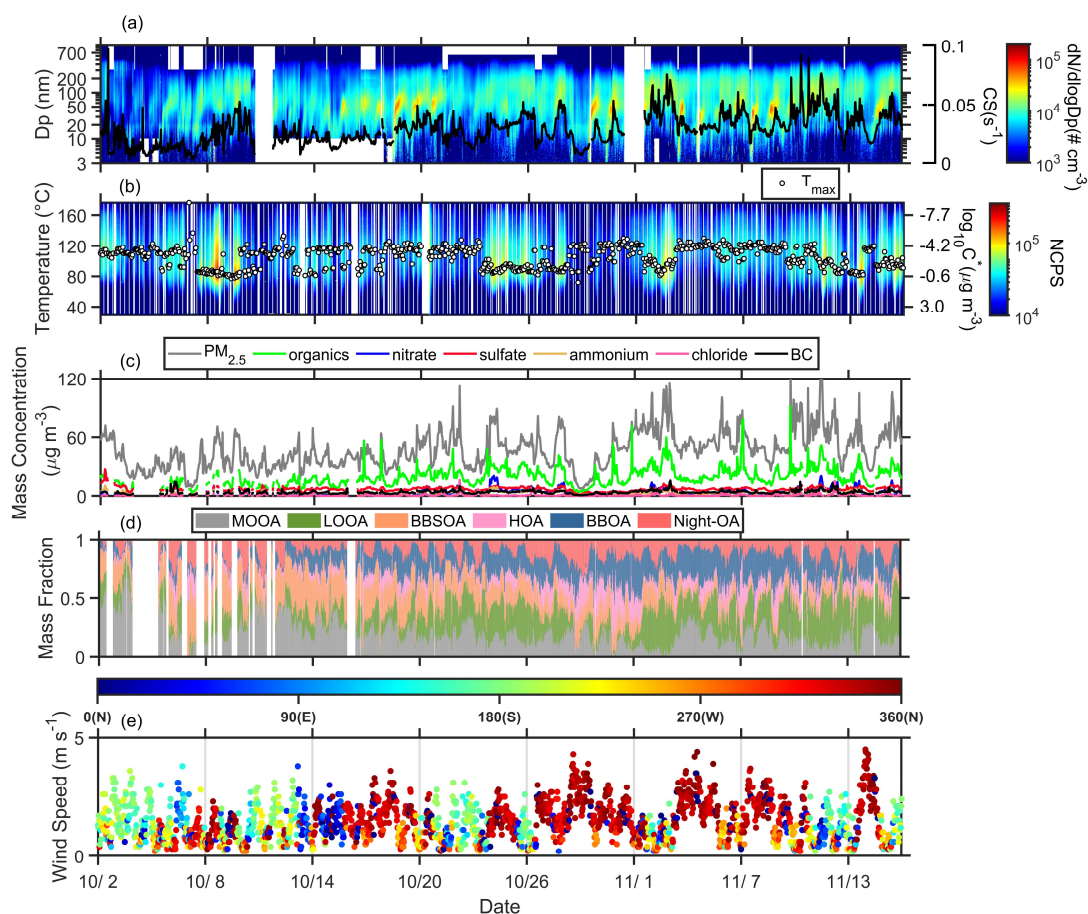792   2019.

793

794

795 **Table 1.** The correlation coefficient between SVOC+LVOC in FIGAERO OA and six OA factors
796 in AMS OA during different periods.

	All campaign	Long-range Transport	Urban Air Masses	Coastal Air Masses
MOOA	-0.004	0.02	0.11	-0.19
LOOA	0.83	0.74	0.85	0.72
BBSOA	0.47	0.48	0.75	0.14
HOA	0.11	0.18	-0.11	0.61
BBOA	0.57	0.55	0.55	0.77
Night-OA	0.35	0.39	0.07	0.53

797
798

799

Figure 1. Temporal profile of the measured variables during the campaign. (a) particle number size distribution and condensation sink (black line); (b) one-dimensional thermograms of organic compounds (ions containing C, H, and O atoms, referred to as sum thermogram) and the T_{max} values (white dots) measured by the FIGAERO-CIMS; (c) bulk PM_1 chemical composition measured by SP-AMS and PM_1 concentration; (d) mass fraction of six OA factors from PMF analysis of SP-AMS data; (e) wind speed and wind direction. The color in (b) represents the normalized count per second (ncps) of oxygenated organic compounds calculated based on total count per second (cps) of oxygenated organic compounds at all m/z ($total\ cps$), m/z 127 (cps_{127}), and m/z 145 (cps_{145}) measured by FIGAERO-I-CIMS, $ncps = \frac{total\ cps}{(cps_{127}+cps_{145})\cdot 10^6}$. The OA factors included more oxygenated OA (MOOA), less oxygenated OA (LOOA), aged biomass burning OA (BBSOA), hydrocarbon-like OA (HOA), biomass burning OA (BBOA), and nighttime OA (night-OA).

814
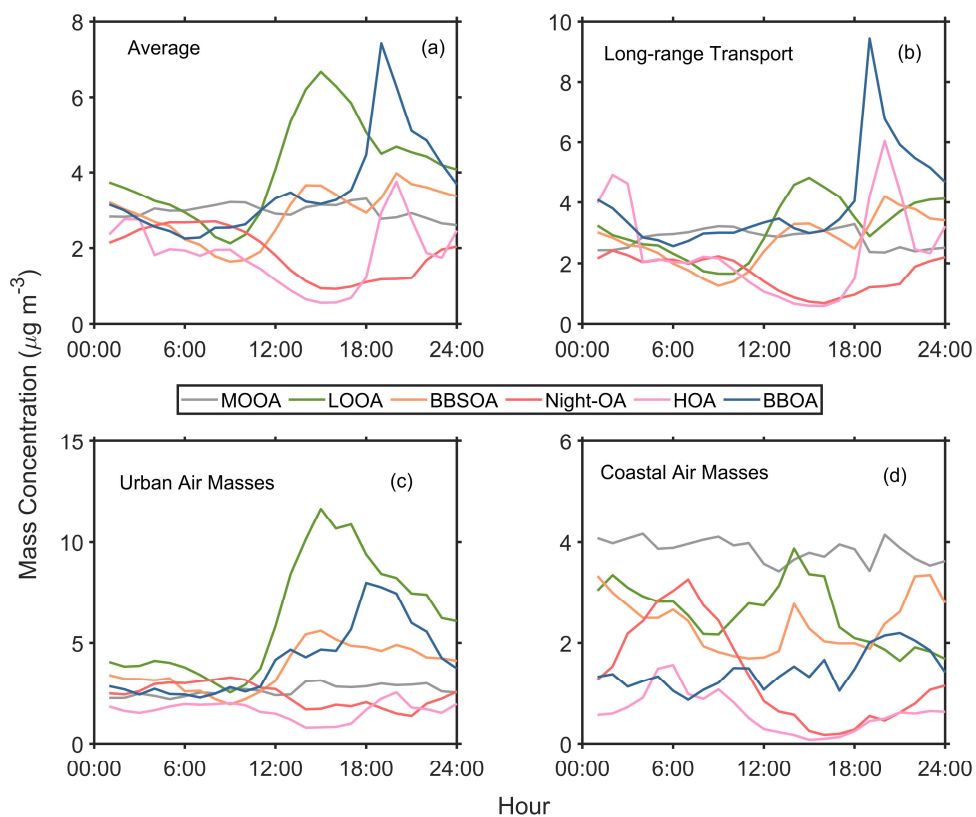
815

816 **Figure 2.** Average diurnal variation of six OA PMF factors during (a) the whole campaign, (b)

817 long-range transport, (c) urban air masses, and (d) coastal air masses periods.

818
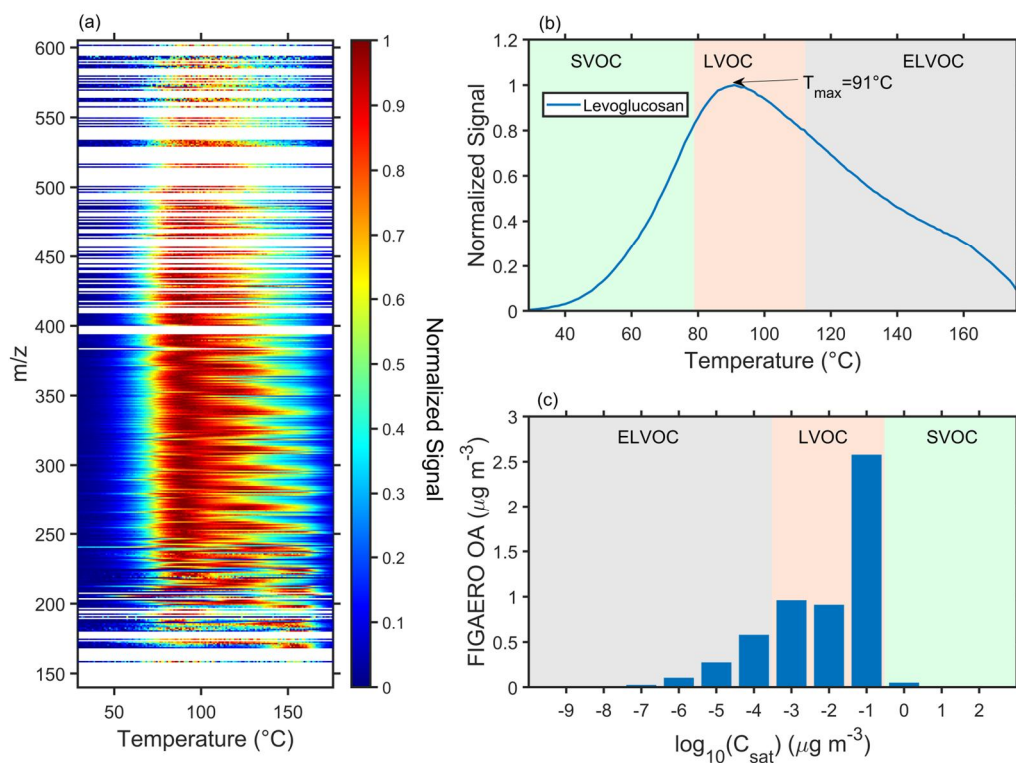
Figure 3. The average (a) two-dimensional thermograms of all calibrated and semi-quantified species, (b) one-dimensional thermogram of levoglucosan, and (c) volatility distribution of all calibration and semi-quantified species in the particle phase measured by the FIGAERO-CIMS (referred as FIGAERO OA). The T_{max} was converted to the C^* according to Eqs. (1) and (2).

823

824
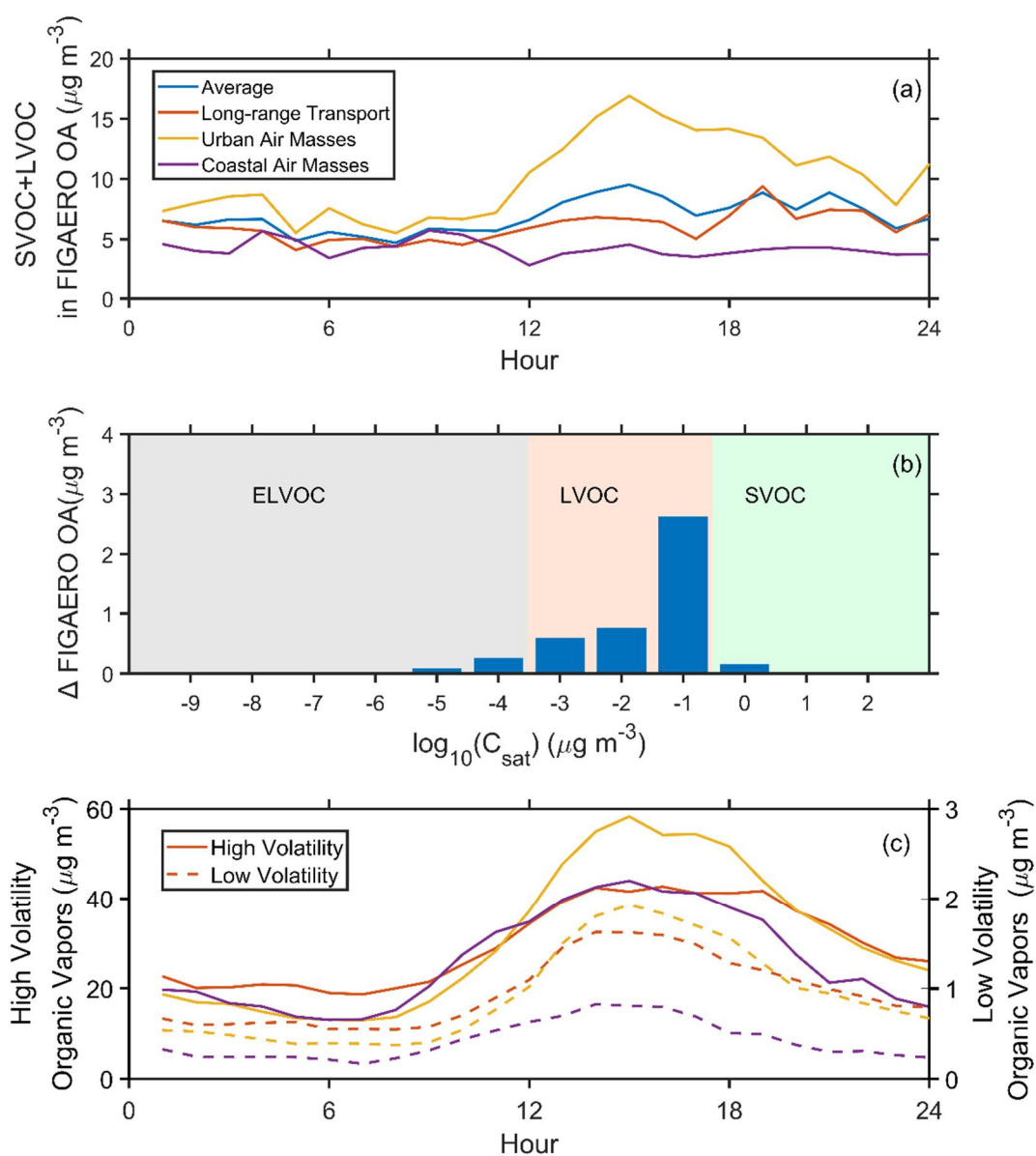
Figure 4. Diurnal variation of (a) SVOC+LVOC in FIGAERO OA, (b) the difference of

FIGAERO OA between the urban air masses and long-range transport periods, and (c) low

volatility organic vapors (ELVOC+LVOC, solid lines) and high volatility organic vapors

(SVOC+IVOC+VOC, dash lines) during the whole campaign and three selected periods.

829
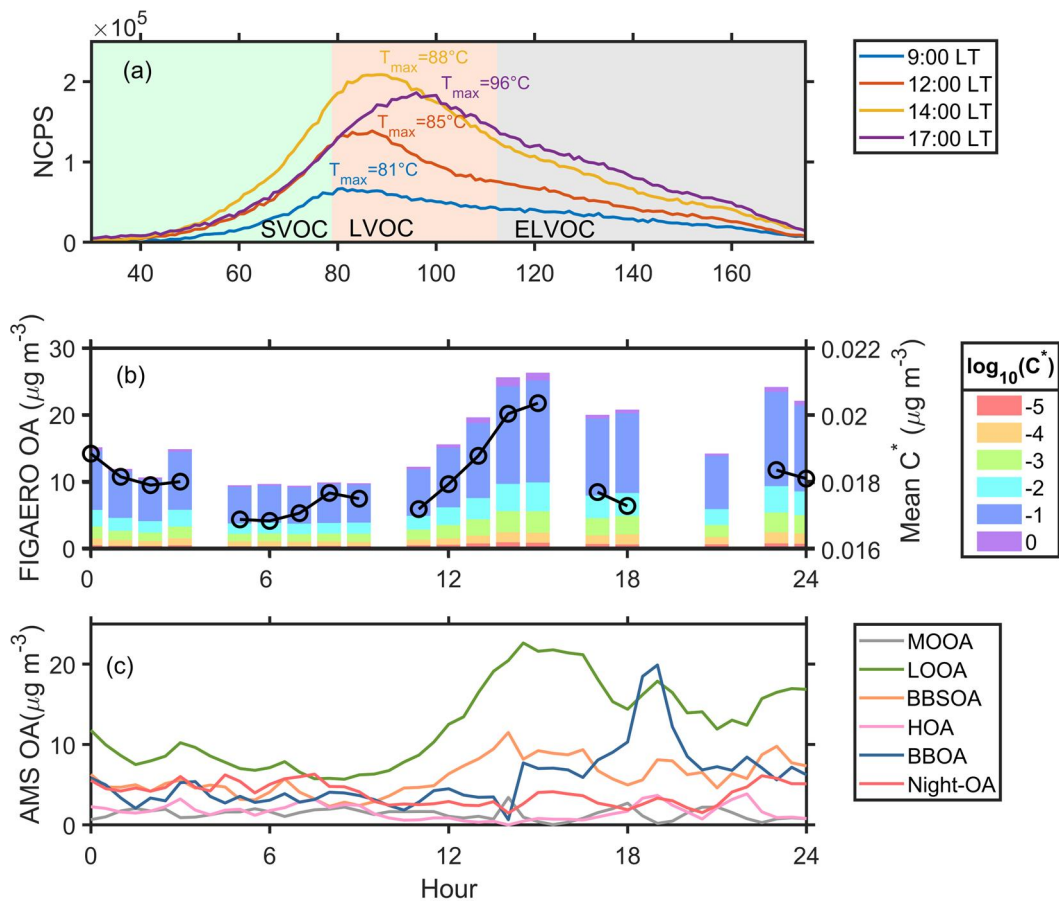
Figure 5. (a) The sum thermograms at 9:00, 12:00, 14:00, and 17:00, (b) variation of FIGAERO

OA volatility presented in a volatility range from 10^{-5} to 10^0 µg m^{-3} and mean C^* , and (c)

variation of six OA factors from PMF analysis on 2 November 2019. The mean $C^*(\overline{C^*})$ is

estimated as $\overline{C^*} = 10^{\Sigma f_i log_{10} C_i^*}$, where f_i is the mass fraction of OA with a volatility C_i^*.
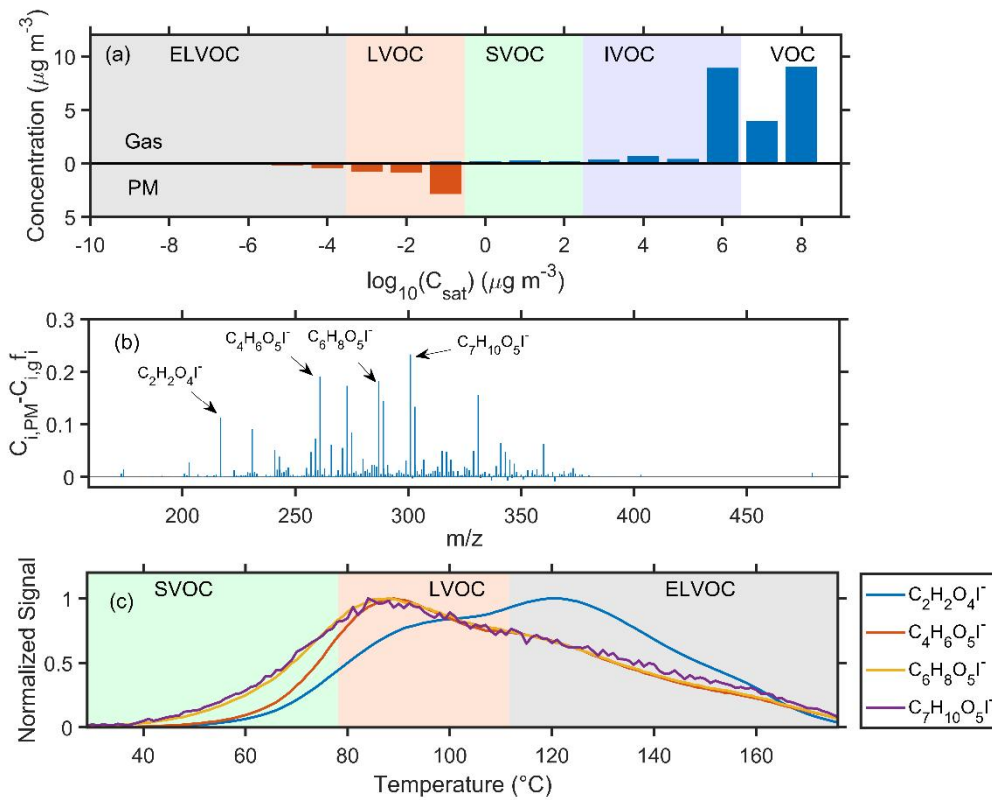
834

835
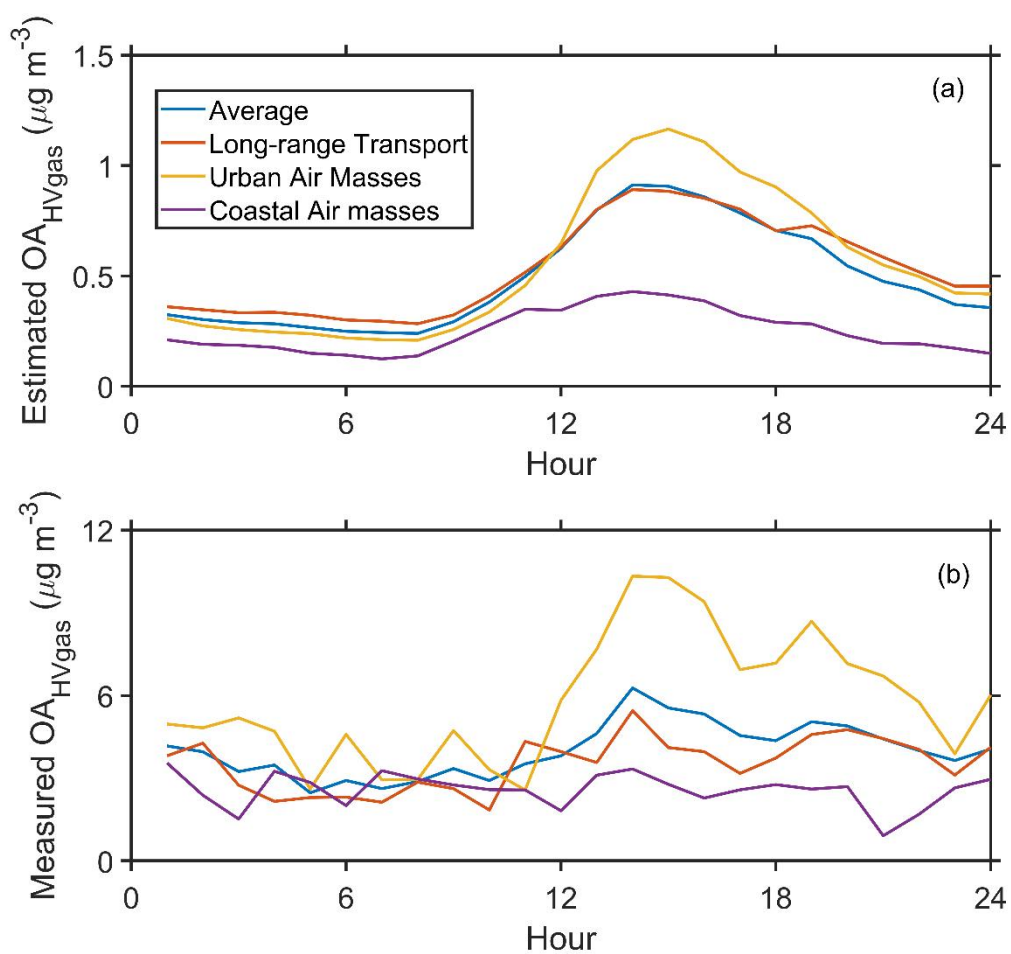
Figure 6. The diurnal variation of (a) the estimated contribution of high volatility organic vapors to the OA (Estimated OA_{HVgas}) and (b) the total concentration of corresponding species in the particles-phase measured by the FIGAERO CIMS.

836

837

838

839

840

Figure 7. (a) The average volatility distribution of high volatility organic vapors in the gas-phase

and particle-phase. (b)The average difference between the measured concentration in the particle-

phase ($C_{i,PM}$) and the estimated concentration ($C_{i,g}f_i$) of different compounds in the high volatility

organic vapors. (c) The average thermograms of $C_2H_2O_4I^-$, $C_4H_6O_5I^-$, $C_6H_8O_5I^-$, and $C_7H_{10}O_5I^-$.

845

846

847
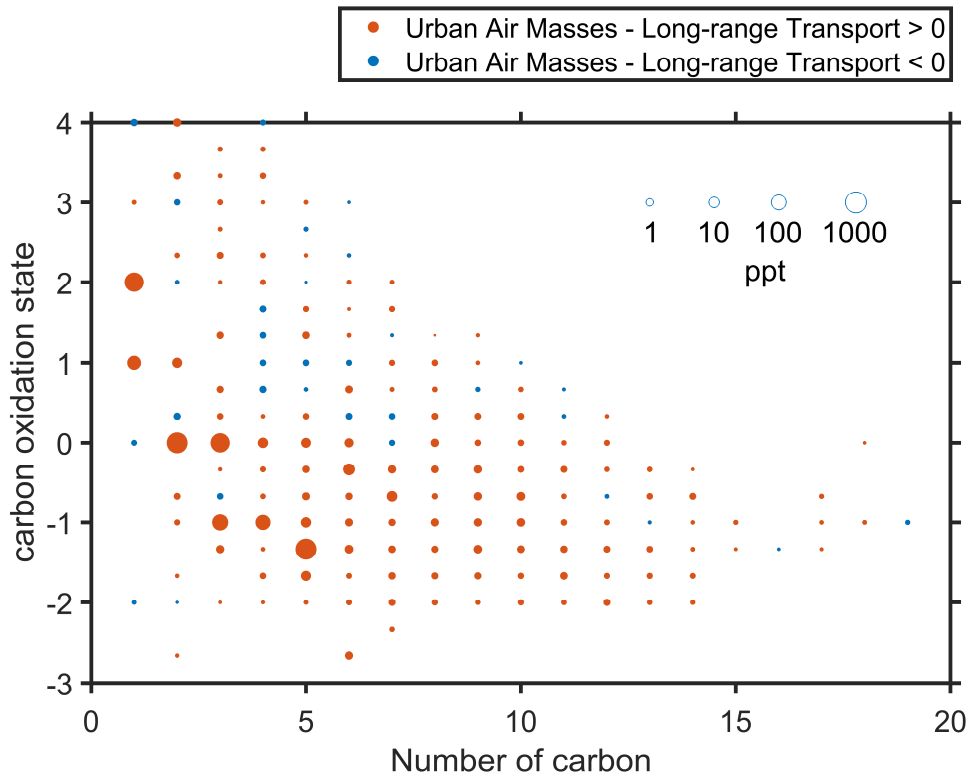
Figure 8. Difference in the carbon oxidation state ($\overline{OS_C}$) in the gas phase in the afternoon (12:00-

16:00 LT) between the long-range transport and urban air masses periods. The symbol sizes are

proportional to the logarithm of concentration. The symbol colors in a and b represent that the

concentration during the urban air masses period was higher (red) or lower (blue) than that during

the long-range transport period.

853
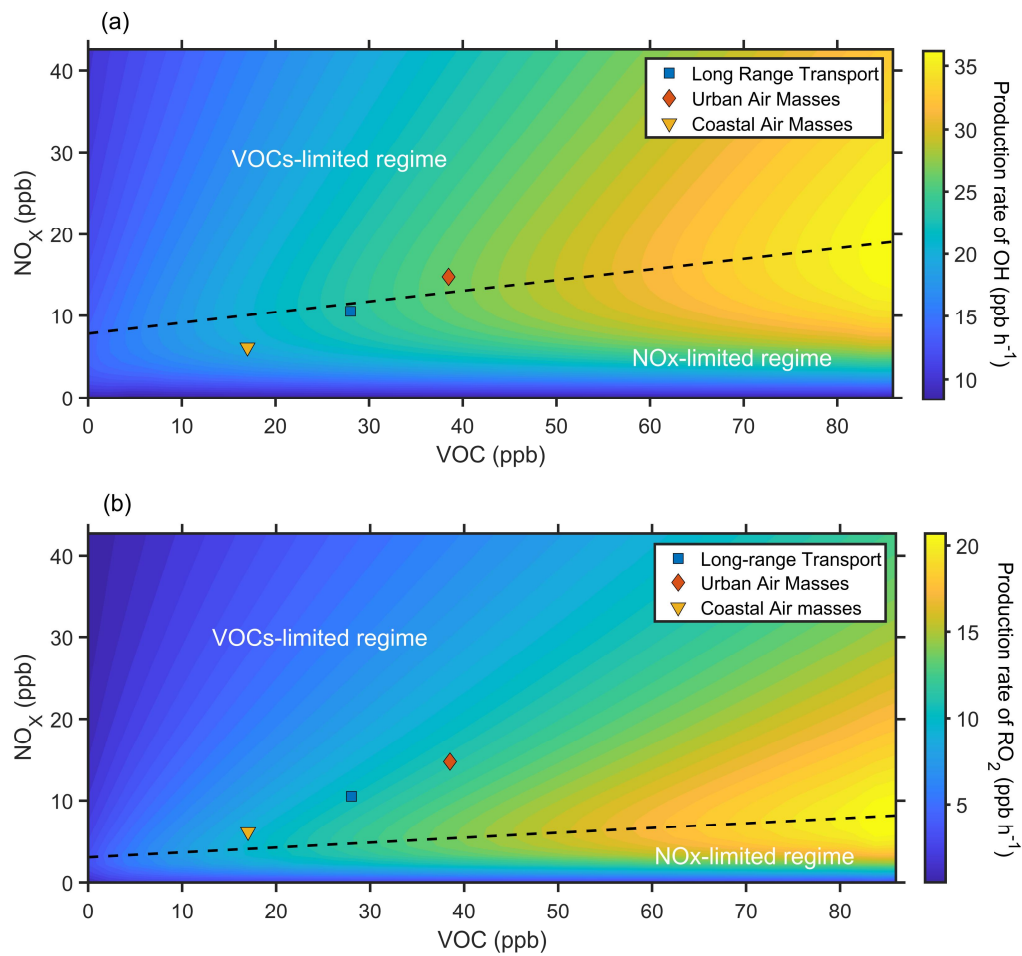
854

855 **Figure 9.** The simulated production rate of OH(a) and RO$_2$(b) with NO$_x$ and VOCs concentration

856 predicted by an observation-constrained box model under campaign average condition. Blue square,

857 red diamond, and yellow triangle represent the average conditions during long-range transport,

858 urban air masses, and coastal air masses period, respectively.

859